

A measurement of absolute efficiency of the ARAPUCA photon detector in Liquid Argon

Dante Totani^a, Gustavo Cancelo^b, Flavio Cavanna^b, Carlos O. Escobar^b, Ernesto Kemp^c, Franciole Marinho^d, Laura Paulucci^e, Dung D. Phan^f, Stuart Mufson^g, Chris Macias^g, and David Warner^h

^aUniversità degli Studi dell'Aquila, L'Aquila, 67100 (ABR), Italia

^bFermi National Accelerator Laboratory, Batavia, IL 60510, USA

^cUniversidade Estadual de Campinas, Campinas - SP, 13083-970, Brazil

^dUniversidade Federal de São Carlos, Araras - SP, 13604-900, Brazil

^eUniversidade Federal do ABC, Santo André - SP, 09210-580, Brazil

^f University of Texas at Austin, Austin, TX 78712, USA

^gIndiana University, Bloomington, IN 47405, USA

^hColorado State University, Fort Collins, CO 80523, USA

November 6, 2019

Abstract

In the Fall of 2017, two photon detector designs for the Deep Underground Neutrino Experiment (DUNE) Far Detector were installed and tested in the TallBo liquid argon (LAr) cryostat at the Proton Assembly (PAB) facility, Fermilab. The designs include two light bars developed at Indiana University and a photon detector based on the ARAPUCA light trap engineered by Colorado State University and Fermilab.

The performance of these devices is determined by analyzing 8 weeks of cosmic ray data. The current paper focuses solely on the ARAPUCA device as the performance of the light bars will be reported separately. The paper briefly describes the ARAPUCA concept, the TallBo setup, and focuses on data analysis and results.

1 Introduction

The efficiency of photon detectors is of paramount importance for large volume LAr experiments. The detection of scintillation light generated as charged particles traverse a large liquid argon time-projection chamber (LArTPC) adds valuable information to the study of weakly-interacting particles. Most importantly, the leading edge of the scintillation light pulse yields sub-mm precision in reconstructing the absolute position of the event in the drift direction [1]. In addition, the scintillation light can provide the trigger for baryon number violation events, such as proton decay and neutron-antineutron oscillations, and supernova neutrinos, as well as improve rejection of uncorrelated cosmic backgrounds. Given the enormous volume of future experiments such as DUNE (Deep Underground Neutrino Experiment) [2], the photon detectors must cover a large surface area in a cost-effective manner. Several technologies and implementations have been proposed and tested. A relatively novel technology is based on a light trapper device designed by A. Machado and E. Segretto named ARAPUCA [3]. ARAPUCAs are able to increase the effective photon collection area while keeping the sensor area small. The latter property allows a relatively high photon collection efficiency at a reasonable cost. The following paper reports on the design and evaluation of a photon detector unit composed of eight ARAPUCA cells. The detector was placed along a photon detector plane that also included two wavelength shifting light guides from the photon detector group at Indiana University [4]. The combined photon detector set operated for eight weeks in the TallBo LAr cryostat at the PAB facility, Fermilab.

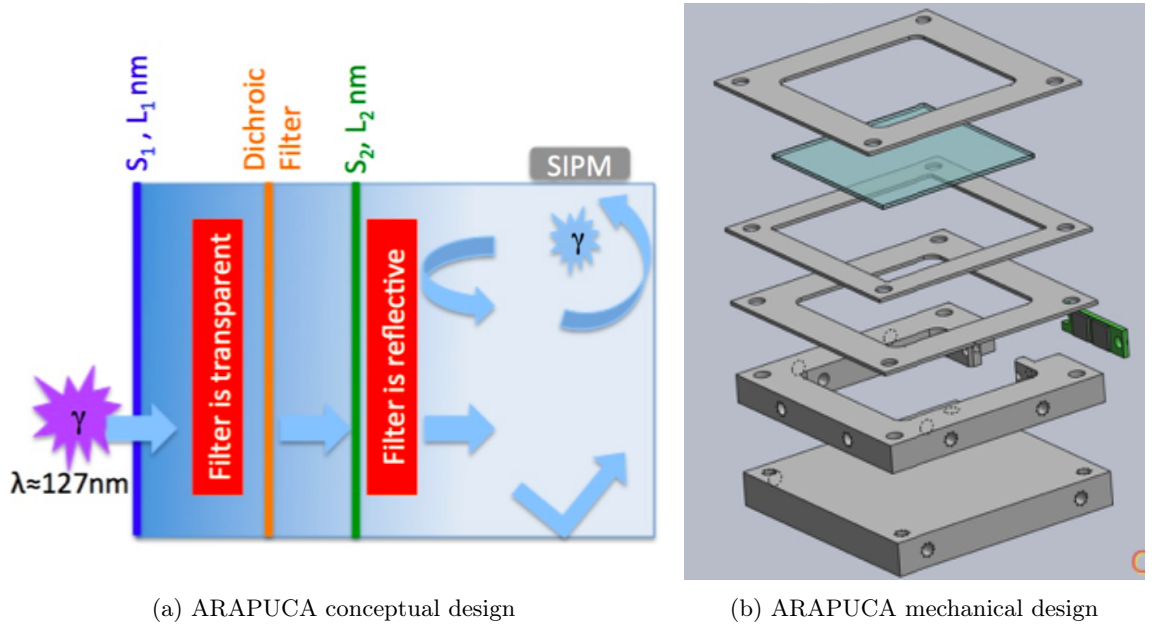


Figure 1: ARAPUCA light trapper device.

1.1 The ARAPUCA Light Trap

The 128 nm scintillation light from interactions of charged particles in LAr is not detectable directly by affordable sensors such as the traditional photomultipliers (PMTs) or the newer silicon photomultipliers (SIPMs) without appropriate wavelength shifter coating. Among available photon detectors, SIPMs are gaining popularity due to its superior quantum efficiency (QE), desired physical and electrical properties as well as a low cost of production. However, due to their small size, their effective light collection area per unit is easily surpassed by PMTs. The ARAPUCA concept [3] brings up a solution to this problem. As shown in Figure 1a the ARAPUCA consists of two wavelength shifters, a dichroic filter, a highly reflective box and photosensors (SIPM). The face of the box is used to augment the photon collection area. The VUV photons that enter the light collecting surface of an ARAPUCA device are wavelength-shifted by $200\mu\text{g}/\text{cm}^2$ of p-terphenyl deposited on the external face of a dichroic filter. The dichroic filter allows the converted photons to go through and enter the box. Those photons are wavelength shifted a second time using $250\mu\text{g}/\text{cm}^2$ of tetra-phenyl butadiene (TPB) deposited on the internal face of the dichroic filter. Since the wavelength cutoff of the dichroic filter is in between the emission spectrum of p-terphenyl and the emission spectrum of TPB, the twice shifted photons remain trapped inside the reflective box and bounce off the walls until they hit the sensors. Figure 1b shows one of the mechanical designs of the ARAPUCA. Several iterations of ARAPUCAs have been studied with variable box sizes, number of SIPMs and location of the SIPMs. In one of the experiments with previous versions of the ARAPUCAs, also performed at TallBo during the Spring 2017 with a radioactive source to excite the LAr, we measured an efficiency $\sim 0.4\%$ [5], considerably lower than the values reported with the new configuration used in this work (see section 3.6). The Fall 2017 TallBo experiment used 8 ARAPUCA units of $9.8\text{cm} \times 7.9\text{cm}$ with 4 SensL $6\text{mm} \times 6\text{mm}$ SIPM biased at 25.5 volts. Figure 2a and 2b show that the emission spectra of p-terphenyl and TPB do not overlap; and the wavelength cutoff of the dichroic filter is located between the two spectra. The peak of the p-terphenyl spectrum is 360 nm, the peak of the TPB spectrum is 430 nm, and the cutoff of the filter is 400 nm.

2 Experimental Setup

2.1 The TallBo cryostat and hodoscope

The vessel's external diameter is 61.82 cm and the inner diameter is 55.88 cm. The full capacity of TallBo is 460 l. For this experiment TallBo was filled with approximately 350 l of liquid argon. The total thickness of stainless steel presented to a cosmic ray particle that crosses the cryostat is

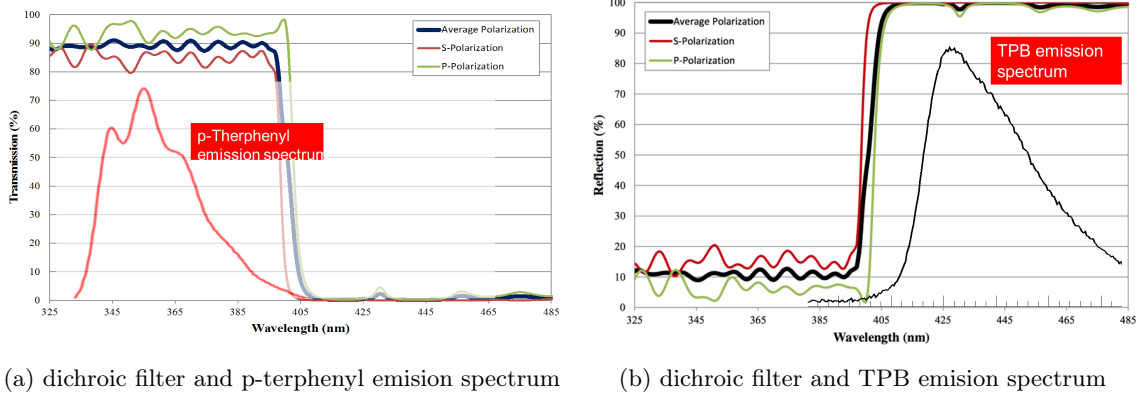


Figure 2: Double coated dichroic filter and wavelength shifter spectra

75 5.08 cm.

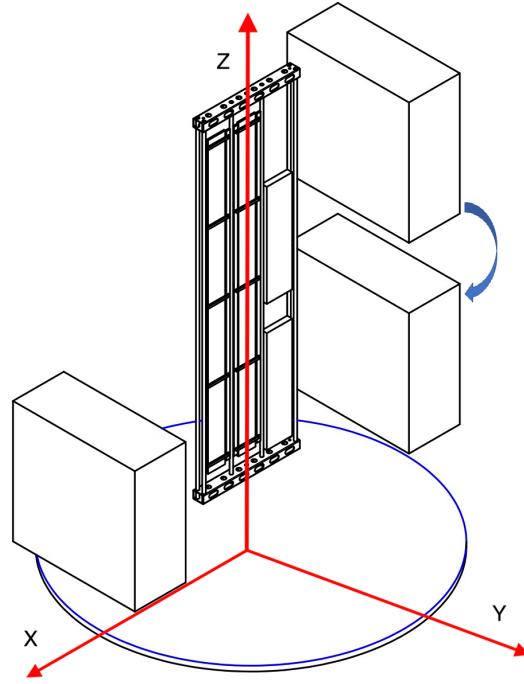
76 The experiment's trigger used a set of two scintillation paddles and a tracking mechanism based
 77 on scintillation paddles and hodoscopes. The hodoscopes were used before in the CREST balloon
 78 flight experiment [6], [7]. The hodoscope modules were installed on opposite sides of the TallBo
 79 cryostat to select single-track cosmic-ray muons passing through the LAr volume [7]. Figure 3a
 80 shows a 3D view of the photon detector plane inside the cryostat and the two hodoscope blocks (in
 81 white), one of which was moved from a high position to a low position to trigger on high angle and low
 82 angle minimum ionizing particles (MIPs) respectively. Each hodoscope module consists of 64 2-inch
 83 diameter barium-fluoride crystals, coated with TPB. Each crystal is monitored by a 2-inch PMT.
 84 The crystals are arranged as 8×8 matrix. Since the hodoscope matrix elements are very sensitive
 85 to extraneous photon activity and have a high dark count rate, to remove extraneous events two
 86 scintillator pannels covering the entire hodoscope face were placed between each hodoscope module
 87 and the TallBo dwear. These panels are individually read out by PMTs. The readout system was
 88 then triggered by four-fold coincidence logic that required at least one hit in both hodoscope modules
 89 as well as one hit in their adjacent scintillator planes in a coincidence window of 150 ns. Events were
 90 further filtered offline by requiring one and only one hit in each hodoscope module to reject showers.
 91 Together triggering on cosmic rays rejecting showers the requirement of having a single crystal fired
 92 per hodoscope module gave geometric position of the tracks. Figure 3b and 3c show, from the top
 93 and from the front of the cryostat, how a track is identified and located by the hodoscope.

94 2.2 The ARAPUCA array

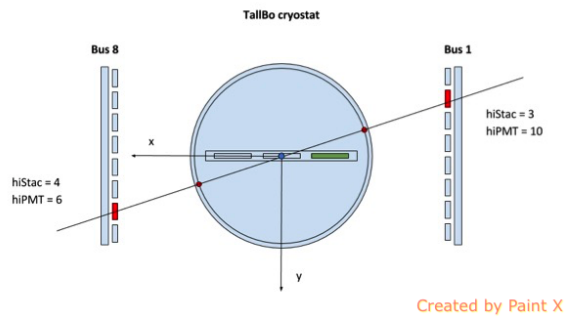
95 As shown in Figure 4, the 8 ARAPUCAs are divided into two frames of 4 ARAPUCAs each and
 96 occupy one third of the photon detector plane. They were located in a side position with respect
 97 to the vertical central axis plane. Each ARAPUCA has dimensions of $12 \text{ cm} \times 9.5 \text{ cm} \times 1 \text{ cm}$. The
 98 filter windows are $10 \text{ cm} \times 8 \text{ cm}$. Two sets of four contiguous ARAPUCAs are placed as shown
 99 separated by a 14.5 cm gap. The values in Figure 4 are given in inches.

100 2.3 Data Acquisition System

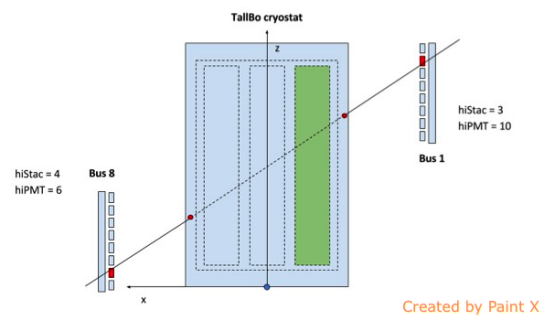
101 Signals are processed by the SiPM Signal Processor (SSP) module designed by the Electronics Group
 102 of the High Energy Physics division at Argonne National Laboratory [8]. The SSP is a 14-bit, 150
 103 MS/s, 12-channel waveform digitizer DAQ. The ADC has a full-scale dynamic range of 2V and a
 104 preamplifier gain of 18.8 V/V. For typical SIPM gains and ganging configurations the SSP allows
 105 large signals equivalent ~ 1000 PEs before the ADC saturates. The SSP input noise is $\sim 16 \mu\text{V}$. Each
 106 acquired waveform contains 1950 ADC values sampled at 150 Ms/s, aggregating to an acquisition
 107 time of 13 μs . The SSP can trigger internally on each individual channel or externally via external
 108 trigger input. The self-trigger mode was used to take calibration data while the external trigger
 109 mode with the hodoscope as the trigger source was employed for the cosmic ray run.



(a) Overall view.



(b) Top view.



(c) Front view.

Figure 3: 3D and cross-sectional views of the TallBo LAr cryostat

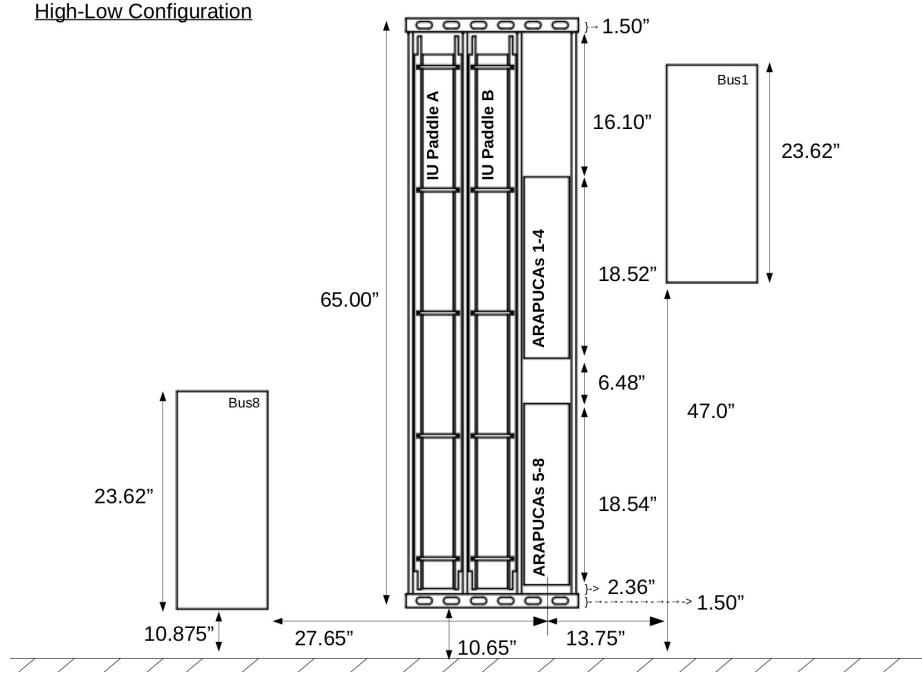


Figure 4: Detector plane configuration.

2.4 Trigger issues

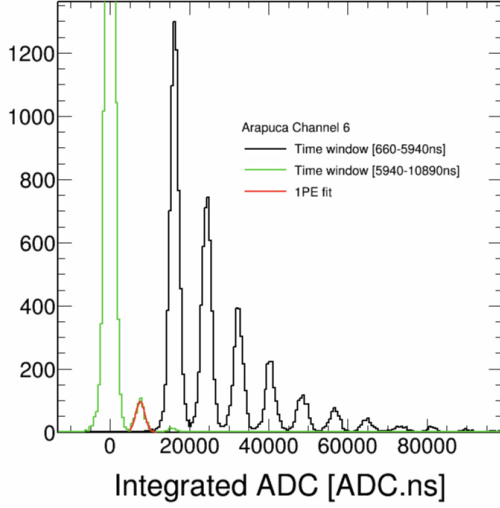
The hodoscope trigger malfunctioned during the experiment. A mistake in the way the coincidence logic was set up caused the trigger to fire more often than expected. The logic performed an OR instead of an AND in two of the channels. Therefore, the trigger not only fired on valid tracks but also on coincidental PMT dark counts of the hodoscope arrays located at the left and right of the dewar during the defined trigger window (150 ns). The collected data set contained a large amount of unusable data that did not represent valid tracks. As shown in the next sections, most of the events were triggered by coincidence of PMT dark counts and contained no signals from the photon detectors, neither in the ARAPUCAs nor the IU light guides. Other spurious events contained partial tracks that did not generate a trigger but were captured by chance during a dark count coincidence event. The hodoscope trigger problem made the analysis of the data challenging, since offline filters had to be devised and applied to the data. However, it also showed the potential of the ARAPUCA architecture given that those filters could have not been applied without the segmentation property of the ARAPUCAs as it will become clear in the next sections of the paper.

3 Data analysis

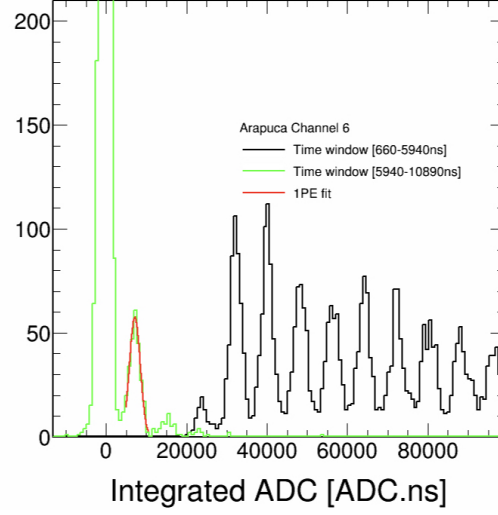
3.1 Calibration

During calibration runs the ARAPUCA signals were acquired by the SSP single channel self trigger mode, using a threshold slightly above 1PE (Figure 5a) and 2 PEs (Figure 5b). Since the two thresholds were higher than the single photon electron the histogram is able to exhibit the 2nd peak and higher (up to 8th PE). The first PE was recovered looking at dark counts in two different integration windows, one starting at 660 ns up to 5940 ns (5280 ns wide) and a second for 5940 ns to 10890 ns (4950 ns wide). Figure 6b shows the linearity of the calibration. Fitting the peaks with Gaussians (Figure 6a) and the distribution of the most probable values with a linear fit (Figure 6b). The integrated charge value ($ADC \cdot ns$) due to one PE can be obtained by the slope of the straight line.

A second procedure was developed to cross check values using the calibration constants obtained from the calibration run. A smaller set of data triggered with the hodoscope was used. Baseline and noise levels were obtained as the mean and root mean square (rms) for the first 100 points of

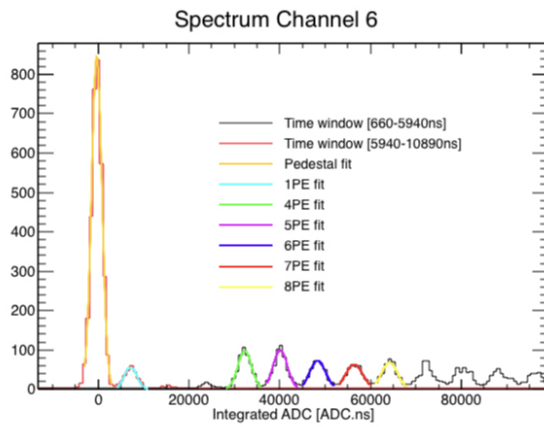


(a) Fit of 1st PE triggering on small signals

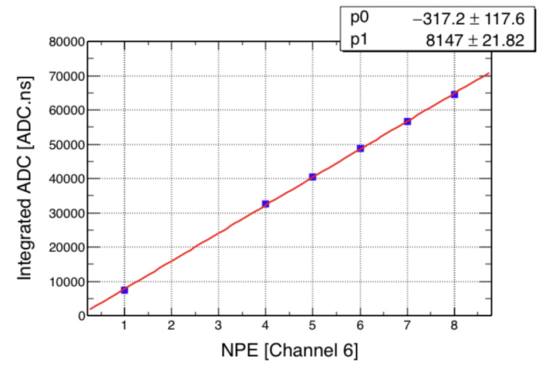


(b) Fit of 1st PE using dark counts

Figure 5: Gaussian fit of 1st PE



(a) Gaussian fits



(b) Linear fit for the peak positions. The slope gives the calibration in $(ADC \cdot ns)/PE$

Figure 6: Gaussian fits of higher order PEs.

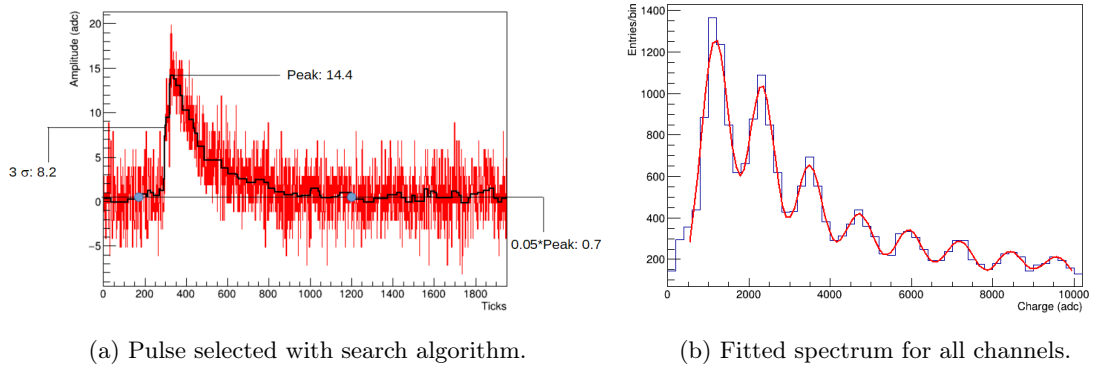


Figure 7: Calibration check with hodoscope triggered data.

the signal amplitude for each channel per event. After baseline subtraction a filtering algorithm was used that suppresses random noise but keeps the main features of the signal, in particular the fast transitions [9]. A peak finding algorithm was then devised to find peaks and integrate the charge under a peak. Figure 7a shows an example of a peak found. The red line shows the raw data and the black line indicates the filtered signal. The threshold for detecting a pulse has been set to 3σ of the baseline noise (e.g. 8.2 ADC). The horizontal lines indicate the height of the peak, the detection threshold used for the search and the blue dots indicate the integration limits for the charge estimate. Figure 7b shows the spectrum obtained with peaks from all channels. Notice that the pedestal is almost suppressed by the denoising procedure and threshold requirement. A multi Gaussian fit was performed to obtain the charge value for each peak. A linear fit of the peaks as a function of the photon electron number provided the average calibration constants which are in agreement with the individual channel analysis.

3.2 Data analysis: background rejection

As mentioned in subsection 2.4 most of the data recorded by the experiment was due to the background, since the majority of the triggers were generated by coincidental dark counts in the hodoscope PMTs. Nevertheless, the system has also properly triggered on real tracks (i.e. MIPs), although these events only constituted a small fraction of the stored data, of the order of 5 to 10%.

Since the dark counts are uncorrelated with light in the cryostat most events of that type were empty or captured incidental background light. Most of these events collected few PEs from radiogenics or very low light background in the TallBo cryostat. A fraction of those events also captured an incidental track that fell within the 150ns trigger window. Most of those tracks are partial tracks that only passed through one hodoscope arm or none at all. In either case the track position information given by the hodoscope is incorrect, since it corresponds to the hot PMTs which generated the trigger and not to the passage of the track.

The tested version of ARAPUCAs were single sided detectors having filters on only one side. Therefore only tracks passing in front of the ARAPUCA plane could be seen. In this particular occasion, due to the high trigger rate, the comparison between the spectra of events passing in front of the single sided ARAPUCAs and behind them was useful to do event discrimination. It was possible to get information comparing the spectra of events triggered as tracks located entirely in front of the plane containing the windows and behind it. That allowed tracks uncorrelated with trigger position information to be filtered out.

As a first step we considered the spectrum of the number of PEs seen by all ARAPUCAs in the detector, for a given event (PE_{tot}). We obtained individual spectra for two groups of events. Group 1 has all events for which the trigger geometry given by the hodoscope labeled a track as passing in front of the ARAPUCA window plane (front events) and Group 2 with all events passing behind the ARAPUCA window plane (back events). Events that have an entry point in the front and the other one in the back or vice-versa were discarded, like the example in Figures 3b and 3c. The spectrum corresponding to tracks labeled by the hodoscope geometry as passing in front of the ARAPUCA detector plane is shown by the blue trace in Figure 8a, the red trace of the same figure displays the back tracks spectrum. The blue (in front) spectra has an excess with respect to the red (back) spectra for a PE range of 600 to 3500. In the range from 0 to 150 PEs, the red spectrum shows an

180 excess over the blue spectrum Figure 8a. The spectra in Figure 8 are plotted in $\log(\text{PE})$ to enhance
 181 the peak display. The difference between the back and front spectra is the only feature which can
 182 be associated to the information coming from the hodoscopes .

183 The spectra shows three peaks, Figure 8a. The first, the largest one, is composed of events for which
 184 two crystals fired but negligible light is seen by any ARAPUCA, indicating these are completely
 185 random triggers, due to the high hodoscope rates. The fact that both back and front spectra show
 186 the first peak identically confirms its origin. The second peak, comprised between 7 PEs and 80
 187 PEs, shows an excess of events in the back spectrum (red). This excess can be associated with a
 188 MIP triggering the crystals for a track located entirely behind the ARAPUCAs plan (back track).
 189 In an equivalent way, the excess of events for the front spectrum (blue) in the third peak, comprised
 190 between 400 PEs and 5000 PEs, can be associated with a MIPs triggering the crystals which gives
 191 a track located entirely in front of the ARAPUCA plane (front track).

192 Comparing the two spectra we can extrapolate the background Figure 8c, as the events which com-
 193 pose the common part, and the events compatible with the hodoscope geometry information for a
 194 track (Figure 8d). The number of events is in a very good agreement with the rate expected from
 195 cosmic ray muon flux through the hodoscopes, obtained analytically, calculating the cosmic ray flux
 196 [10] through the hodoscope geometry getting 0.011 Hz and doing a simulation of the muons crossing
 197 the hodoscope: 0.0105 Hz . The total number of selected events between 400 PEs and 5000 PEs is
 198 13005 events, Figure 8d. That number is the total for 366 hours of running time at a rate of 0.010 Hz .
 199

200 When the front and back labeled tracks are plotted for each individual ARAPUCA we find
 201 spectra as depicted in Figure 10, shown in log scale for better visualization. Applying cuts on the
 202 minimum and maximum number of PEs collected by the ARAPUCAs based on front versus back
 203 spectrum discrimination we are left with 14,811 events. The cut consist in removing events for which
 204 the back spectra (red in 10) has more events respect the front spectra (blue in 10). An example is
 205 shown in Figure 9. This is a crude cut, so we expect that the remaining data set is still contaminated
 206 with background. The next step in background rejection utilizes another important feature of the
 207 ARAPUCA, the segmentation of the detector given by the 8 ARAPUCA cells.

208 3.3 ARAPUCAs multi-channel information

209 Each ARAPUCA is read out by an independent SSP channel, the segmented information can be
 210 used to study the track geometry. The number of PEs measured by each ARAPUCA must match
 211 the profile of the expected number of photons hitting the ARAPUCA array given a track geometry,
 212 with the track geometry provided by the hodoscope. The ratio between the number of PEs col-
 213 lected and the number of photons hitting each ARAPUCA depends only by their intrinsic features
 214 (geometrical dimensions, number of SiPM, wavelength shifter, dichroic filter). It should be constant
 215 and independent of the track geometry and the number of photons generated by a track in the LAr.
 216 Inconsistency of these ratio means we are observing a track not compatible with the geometry pro-
 217 vided by the hodoscope. In that experiment the 8 cells of which the ARAPUCA array is composed,
 218 have the same features so we expect them to behave in the same way. The determination of the
 219 number of photons hitting each ARAPUCA is shown in the next section.

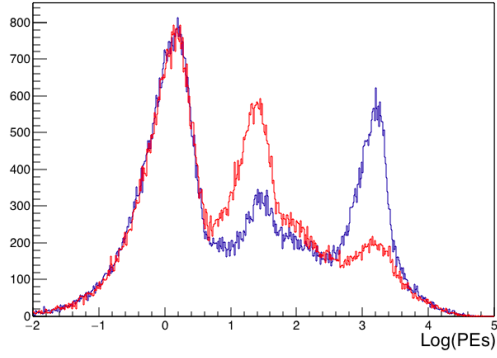
220 3.4 Light pattern

221 A charged particle crossing the volume of liquid argon will generate an amount of scintillation
 222 photons per unit of track length given by:

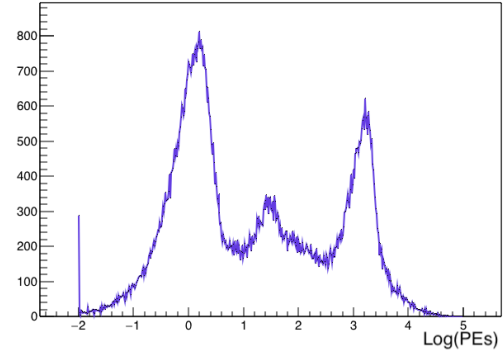
$$\frac{dN^\gamma}{dl} = \left\langle \frac{dE}{dx} \right\rangle \rho Y_\gamma q_p, \quad (1)$$

223 where $\left\langle \frac{dE}{dx} \right\rangle$ is the specific deposited energy (MeVcm^2/g), ρ is the density of the liquid in which
 224 the particle travels (g/cm^3), Y_γ is the number of photons emitted per unit deposited energy in the
 225 medium (γ/MeV), and q_p is the quenching factor [11, 12]. A crossing muon was assumed to be a
 226 MIP with a photon yield in liquid argon of 4×10^4 photons/MeV and an energy deposit $\left\langle \frac{dE}{dx} \right\rangle \rho$ of
 227 2.12 MeV/cm.

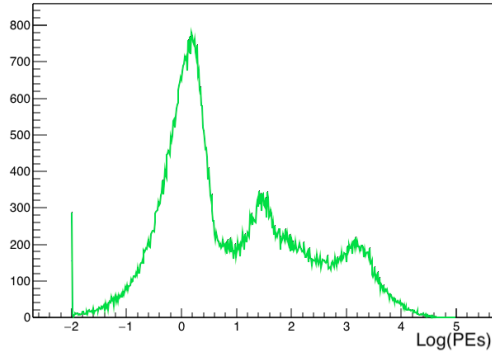
228 The number of photons that arrive at the detector window due to a muon passing the argon
 229 volume is estimated as the product of the track integrated angular acceptance, A_Ω , and the number
 230 of emitted photons per unit length. This acceptance is defined numerically as:



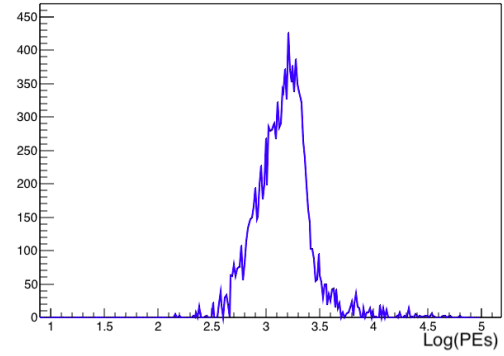
(a) Histogram of $\text{Log}(\text{PETot})$ of the two spectra.



(b) Total $\text{Log}(\text{PE})$ spectra for front triggers.



(c) Extrapolated background for front tracks.



(d) Extrapolated good events for front triggers.

Figure 8: (a), show the PE spectra for events triggered as "front" (blue) and "back" (red). The difference between the front and the back spectra are the events associated with a track given by the trigger information. All common parts of the spectra are considered background since they appear both for events triggered as back tracks and for events triggered as front tracks. Figure (b) shows the event distribution for front triggers as a function of the logarithm (base 10) of the number of photon electrons. Figure (c) and (d) show the same distribution but now for the extrapolated background and the extrapolated good events, respectively. Figure (d) shows the $\text{Log}(\text{PETot})$ spectrum in order to make more evident the range of the bump from 400 ($\text{Log}(400)=2.6$) to 5000 PE ($\text{Log}(5000)=3.7$) in Figure (a).

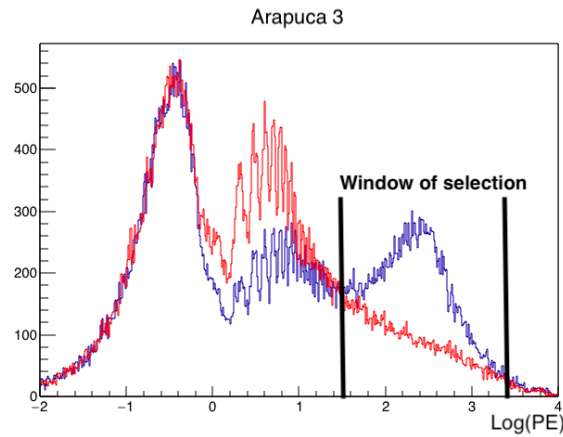


Figure 9: Example of the cut applied for Arapuca 3

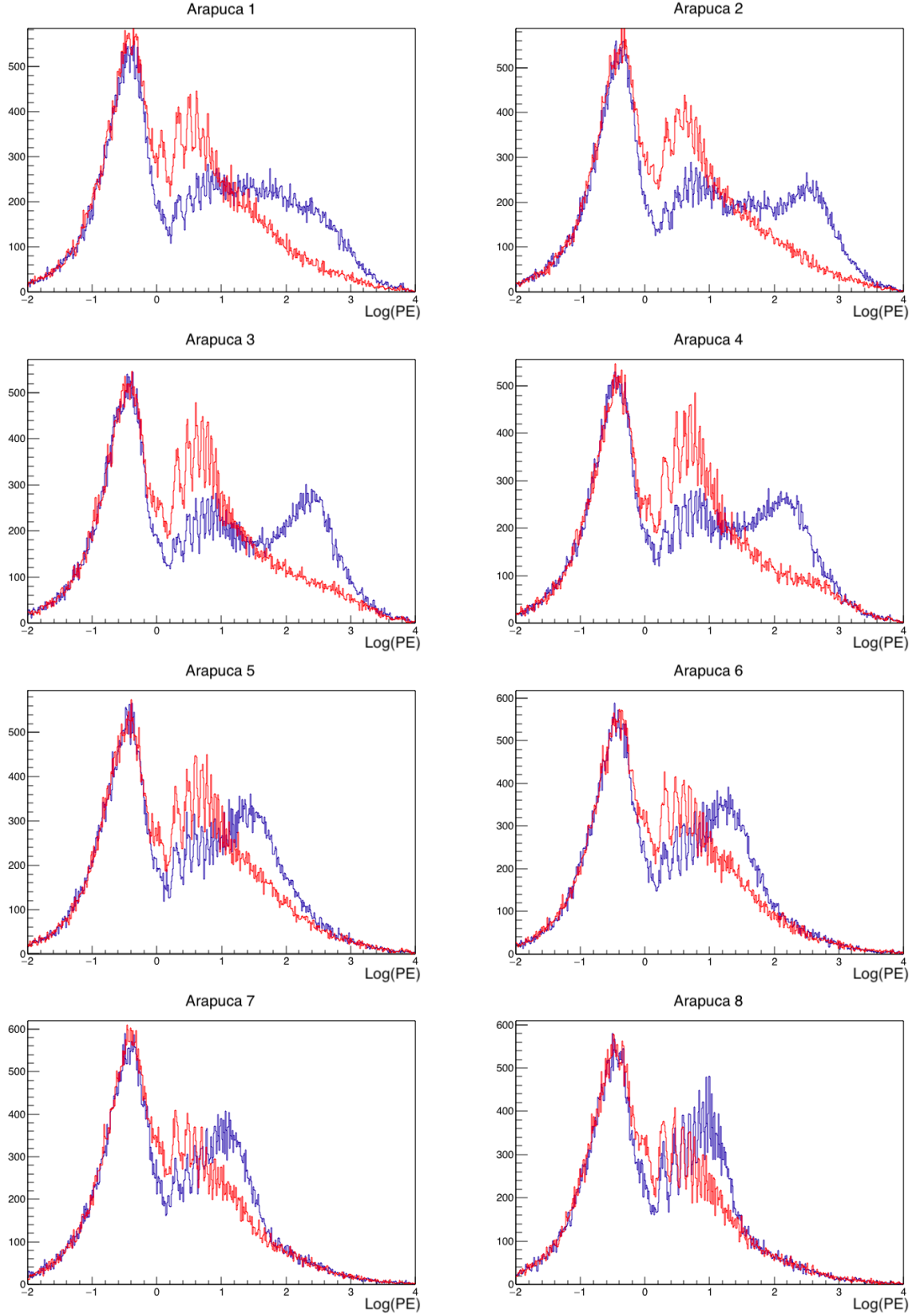


Figure 10: Front (blue) and back (red) spectra for the eight ARAPUCAs. The parts of the spectra which do not overlap are the events associated with a back and front events. The common part can be associated with the background from spurious hodoscope coincidences since it appears with the same distribution for both: events triggered as back and events triggered as front.

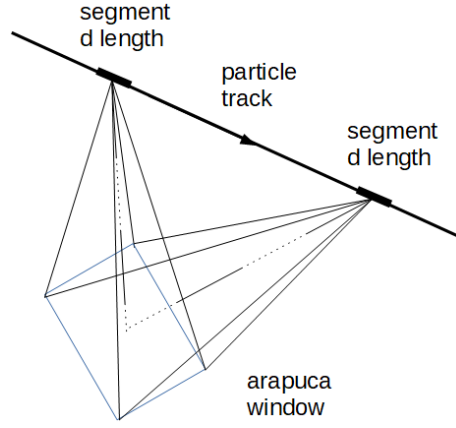


Figure 11: Track angular acceptance.

$$A_{\Omega} = d \sum_{i=1}^N \Omega_i, \quad (2)$$

where d is the length of a small (i.e. differential) segment of the muon trajectory and Ω_i is the solid angle of the pyramid with its apex at the center of that segment and its base given by the sensor window.

Ω_i is calculated using a set of formulas given in reference [13]. Figure 11 illustrates track segments and their correspondent Ω_i .

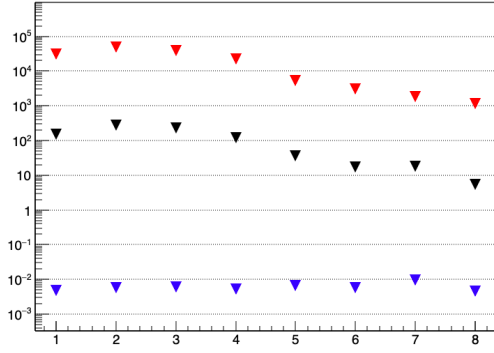
The total number of photons arriving at the ARAPUCA window is obtained as:

$$N^{hit} = \frac{1}{4\pi} A_{\Omega} \frac{dN^{\gamma}}{dl}. \quad (3)$$

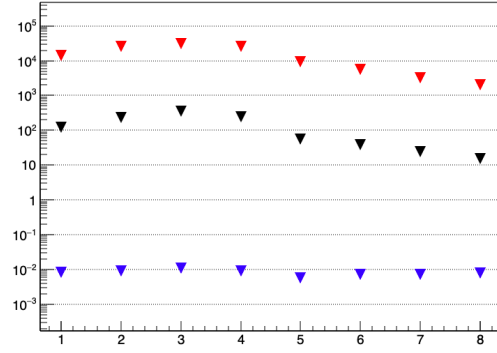
The expected light calculated by the formulas and the number of PEs measured were compared, as displayed in fig. 12 for a few example tracks. There is a reduced set of events for which the expected and detected light follow the same shape pattern. It is expected that the absolute efficiency per ARAPUCA is a constant number smaller than 1. As mentioned previously, the efficiency is defined as the ratio between the number of PEs collected by the ARAPUCA and the number of photons arriving at the ARAPUCA window for a valid track event. Figure 12 demonstrates, for a valid track (a), the remarkable discrimination power of the ARAPUCA showing how the distribution of the collected light closely follows that expected for the illumination light, scaled down by a constant smaller than one that is directly related to the efficiency of the device. Also, for a different valid track such as in (b), that constant must remain the same within errors. Furthermore, (a) and b) show that the ratios are similar for the 8 ARAPUCAs used in the experiment. Figure 12 (c) and (d) also show that the same discrimination power allows filtering events where the shape of the distribution of the light collected by the ARAPUCAs do not follow that of the expected illumination. These tracks are due to MIPs that partially illuminated the ARAPUCAs and were mistakenly catalogued by the hodoscope with the wrong geometry due to hot PMTs and coincidental PMT events. The criteria to separate valid from invalid tracks followed a χ^2 requirement as explained in the following section.

3.5 Correlation between collected and expected light.

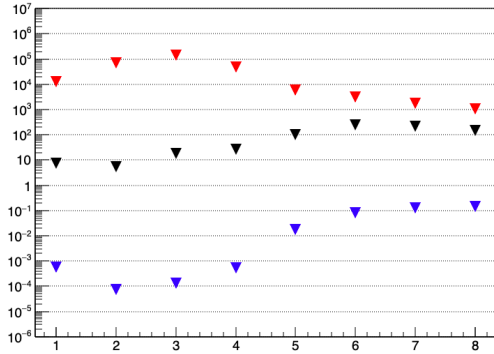
Comparing the amount of expected light coming from the analytical formula and the number of PEs from waveforms, leads us to the determination of good tracks. In Figure 12 the number of PEs measured (black), the number of landing photons (PH, in red), and their ratio (blue) are displayed for each ARAPUCA, for a few tracks. There is a reduced set of events for which the expected and detected light follow the same pattern Figure 12a and Figure 12b. As an estimator for light pattern information we used the correlation between the measured PE number and the calculated number of photons landing on the ARAPUCA for each ARAPUCA in the event. The measure of correlation



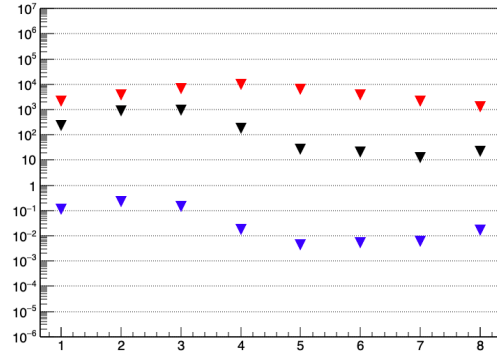
(a)



(b)



(c)



(d)

Figure 12: Comparison between the amount of light expected to arrive in each ARAPUCA (red), the number of PEs extracted from the waveforms (black) and the ratio between them (blue). Figures (a) and (b) show events following the pattern expected, Figures (c) and (d) show events not correlated with the trigger information. Blue points show the ratio of measured to expected number of photons.

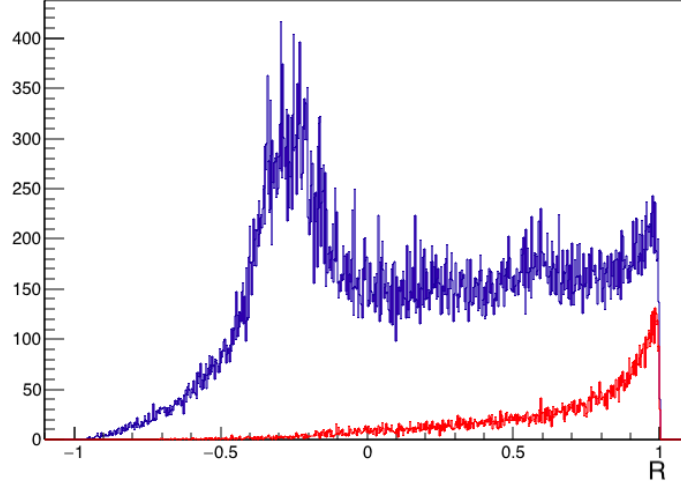


Figure 13: Correlation between PE_i and PH_i for the eight ARAPUCAs. Blue is for all the events, red for the events with the PE numbers, recorded by each ARAPUCA, in the range determined from the back and front spectra analysis.

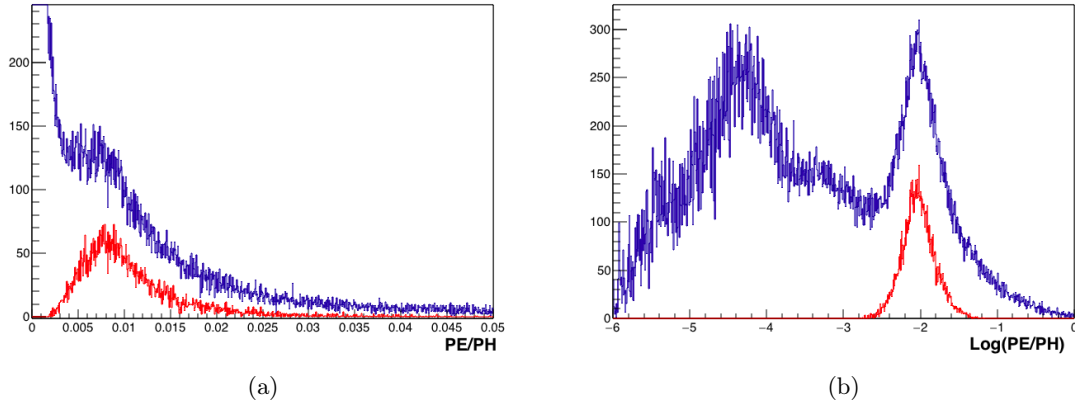


Figure 14: Ratio between the sum of the photo electrons measured and the sum of the estimated number of arriving photons per each ARAPUCA (left) and its logarithm (right). Blue spectra are all data, red spectra are data after the cuts.

used is given by the Pearson correlation coefficient defined as

$$C = \frac{\sum (PE_i \cdot PH_i) - \sum PE_i \cdot \sum PH_i / 8}{\sqrt{\sum (PE_i^2) - (\sum PE_i)^2 / 8} \cdot \sqrt{\sum (PH_i^2) - (\sum PH_i)^2 / 8}} \quad (4)$$

Figure 13 shows the correlation parameter for the total number of events (blue) and for the events passing the cut on the spectra (red). Most of the events passing the cut are peaked around $C = 1$ indicating a good correlation between the eight ARAPUCAs. However there are some events with $C \leq 0$. A second cut on the correlation parameter is done, selecting the events with $C \geq 0.7$.

3.6 Efficiency analysis

The selected data set is then used to perform the efficiency analysis. The efficiency is defined as the ratio between the number of measured photons and the estimated number of arriving photons for each ARAPUCA:

$$\mathcal{R}_i = \frac{PE_i}{PH_i} \quad (5)$$

ARAPUCA	Mean (%)	Median (%) Fit result	Median (%) Robust stat.	MAD (%)
TOT	0.78 ± 0.02	0.80	0.77	0.41
1	0.74 ± 0.02	0.80	0.75	0.46
2	0.77 ± 0.02	0.85	0.80	0.55
3	0.80 ± 0.02	0.84	0.77	0.55
4	0.77 ± 0.02	0.71	0.66	0.42
5	0.75 ± 0.02	0.67	0.64	0.35
6	0.77 ± 0.02	0.69	0.65	0.36
7	0.77 ± 0.02	0.70	0.67	0.37
8	0.80 ± 0.02	0.80	0.75	0.40

Table 1: Ratio values from the three analysis. The error on the fit parameter associated to the median is negligible.

Figure 15 shows the ratio distribution for the eight channels. Furthermore, the ratio between the sum of the number of photoelectrons collected by all ARAPUCAs divided by the sum of the number of expected photons landing on all ARAPUCAs is considered. In figure 14 is reported \mathcal{R}_{TOT} and $\text{Log}(\mathcal{R}_{TOT})$ for better visualization.

$$\mathcal{R}_{TOT} = \frac{\sum_{i=1}^8 PE_i}{\sum_{i=1}^8 PH_i} \quad (6)$$

Three metrics for analysis were used, finding similar results reported in table 1:

- log-normal fit
- robust statistic
- bootstrap procedure on a reduced dataset

Details about the performance of each metric can be found in the Appendix.

A second criteria of data selection, based on a χ^2 requirement on the ratio \mathcal{R}_i , was applied to the original dataset to check the goodness of the cuts.

$$\Sigma = \frac{1}{8} \sum_{i=1}^8 \left(\frac{\mathcal{R}_i - \mathcal{R}_{TOT}}{\mathcal{R}_i + \mathcal{R}_{TOT}} \right)^2 \quad (7)$$

Requiring a condition on Σ we can select a certain amount of events. A smaller Σ means a better match between collected and expected photons. The conditions on Σ were determined in order to get the same amount of data of the other cuts, and the same three analysis were performed: robust statistic and log normal fit for a dataset using $\Sigma < 0.1$ and bootstrap procedure for a dataset using $\Sigma < 0.02$. Table 1 displays the ARAPUCA efficiency values measured by all metrics.

A similar analysis was made for the Low-Low hodoscope configuration using 3 MeV/cm of energy loss, reflecting the fact that the average muon energy increases for more horizontal events [14]. Due to the geometry of the tracks only the lower four ARAPUCAs are taken into account. The upper four have a small acceptance. The ratio \mathcal{R}_i (Eq. 5) is affected by large fluctuations because the number of photons detected is dominated by Poisson statistics. Table 2 shows the results from the two selection criteria for the two configurations. The ARAPUCA efficiency given by the median of the individual cells is $\mathcal{R} = (0.77 \pm 0.02)\%$. The TallBo7 test did not provide a measurement of after pulse and cross talk. The efficiency values reported here do not take into account their contribution. However, an estimation of $(31 \pm 7)\%$ of after pulse and cross talk is obtained from ProtoDUNE [15] preliminary analysis, where the same kind of SiPM were used and run in similar bias conditions. Adjusting by 31% the detection efficiency of the ARAPUCA detectors becomes $\epsilon = (0.60 \pm 0.02)\%$.

4 Conclusions

The Fall 2017 TallBo experiment has been successful in testing ARAPUCA photon detectors. Two of the features of the current ARAPUCA photon detector design were used to be able to filter the

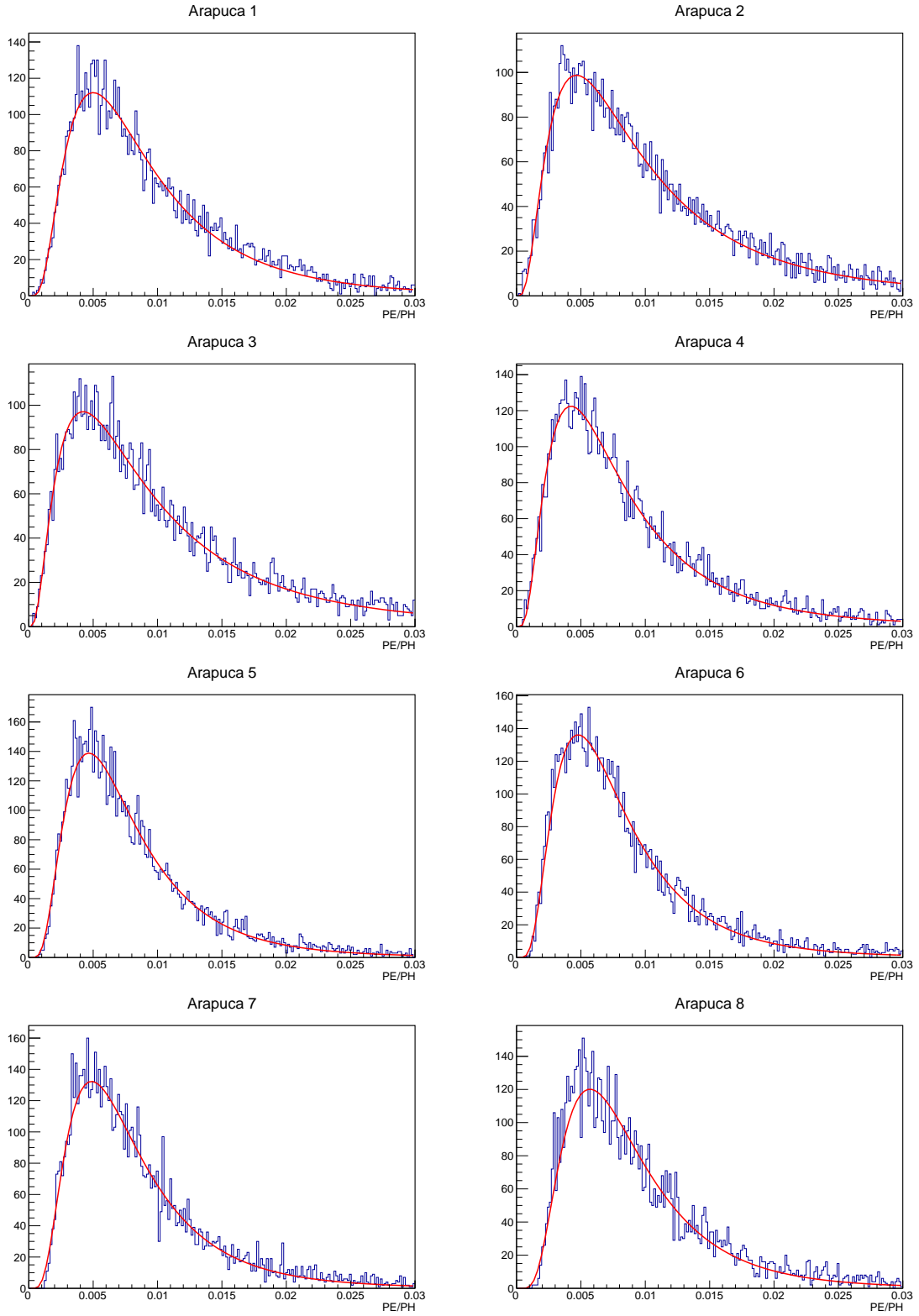


Figure 15: Ratio between the photo electrons measured and the estimated number of arriving photons per each ARAPUCA.

ARAPUCA	Hi-Low Cut 1	Low-Low Cut 1	Hi-Low Cut 2	Low-Low Cut 2
TOT	0.78 ± 0.02	0.78 ± 0.02	0.75 ± 0.01	0.75 ± 0.03
1	0.74 ± 0.02	-	0.72 ± 0.01	-
2	0.77 ± 0.02	-	0.75 ± 0.01	-
3	0.80 ± 0.02	-	0.77 ± 0.01	-
4	0.77 ± 0.02	-	0.74 ± 0.01	-
5	0.75 ± 0.02	0.81 ± 0.02	0.73 ± 0.01	0.75 ± 0.04
6	0.77 ± 0.02	0.75 ± 0.02	0.75 ± 0.01	0.78 ± 0.04
7	0.77 ± 0.02	0.72 ± 0.02	0.76 ± 0.01	0.78 ± 0.04
8	0.80 ± 0.02	0.79 ± 0.02	0.80 ± 0.01	0.79 ± 0.04

Table 2

data offline. The single face detection and the fine segmentation of the ARAPUCAs allowed the offline analysis to separate events from background. The segmentation of the ARAPUCA detector validated the geometry given by the hodoscope. In the end an accurate absolute efficiency of 0.6% was determined by three different methods. That absolute efficiency is higher than efficiency measurements reported by previous experiments at TallBo using scintillation bars and wavelength shifters.

It is also worth mentioning that the ARAPUCAs only used 4 SiPMs per board, the filter to sensor aspect ratio was 35 which shows a remarkable improvement in the equivalent photon collection area given by the light-trap effect in the ARAPUCA.

Future work will study improvements in the internal reflective surfaces of the ARAPUCA, wavelength shifter thickness and adherence which should help increasing the light collection. A step forward in the development of ARAPUCA is the active ganging of SiPMs to lower the number of readout channels per module and the use of the two faces of the detector for photon detection, having filters on both sides.

A Appendix

A.1 Log-normal fit

A first analysis is made by fitting the ratio distribution with a Log-Normal distribution:

$$f(x) = \frac{1}{x\sigma\sqrt{2\pi}} e^{-\frac{(\ln(x)-\mu)^2}{2\sigma^2}} \quad (8)$$

This choice is driven by the $\text{Log}(\mathcal{R}_{TOT})$ which seems to follow a Gaussian distribution. The values of the Mean, Median, Mode, Variance and Standard Deviation are obtained by the relations satisfied by the parameters of the Log-Normal distribution:

- Mean: $e^{(\mu + \frac{\sigma^2}{2})}$
- Median: e^μ
- Mode: $e^{(\mu - \sigma^2)}$
- Variance: $(e^{\sigma^2} - 1) e^{(2\mu + \sigma^2)}$
- Standard Deviation: $\sqrt{(e^{\sigma^2} - 1)} e^{(\mu + \frac{\sigma^2}{2})}$

The error propagation, from the error in the fit, gives for the median the value:

$$\Delta_{Median} = e^\mu \cdot \Delta_{mu} \quad (9)$$

328 A.2 Robust statistic

329 Because of the presence of outlier events, such as the ones in the far tail of the spectrum, a robust
 330 statistic data analysis is made for the data relative to the single ARAPUCA (\mathcal{R}_i) and their sum
 331 (\mathcal{R}_{TOT}), using median and the median absolute deviation (MAD) to build a robust score defined
 332 as:

$$\mathcal{S}_i = \frac{(\mathcal{R}_i - \text{median}_{j=1,\dots,n}(\mathcal{R}_j))}{MAD} \quad (10)$$

333 Then the median of the data set composed by the data which passes the requirement $\mathcal{S}_i < 2.5$ is
 334 calculated..
 335

336 A.3 Strong correlation

337 Finally a restricted data set, obtained with a further strong condition on the light pattern, is
 338 analyzed.

339 The strong condition consists in requiring that all ARAPUCAs have the ratio \mathcal{R}_i similar to each
 340 other:

$$\frac{1}{2} \cdot \mathcal{R}_j \leq \mathcal{R}_i \leq 2 \cdot \mathcal{R}_j \quad (11)$$

341 This condition reduces the data set to be $\sim 10\%$ of the one used in the previous two analysis.
 342 A bootstrap procedure is used to find the average values of the ratio and its errors, generating 10
 343 thousand data sets, each of them composed by random extraction of events, from the original data
 344 set.

345 B Acknowledgements

346 The authors would like to thank R. P. Davis, W. Miner, K. Harding for their technical support
 347 at PAB. We also thank Stuart Mufson and the whole Indiana University team with whom this
 348 experiment was performed. We also thank Eileen Hahn for her invaluable knowledge and support
 349 for the wavelength shifter coatings of filters and reflectors, and also Kenneth Treptow for his technical
 350 support in assembling the ARAPUCA's module. This work has been partially supported by the
 351 Brazilian agency FAPESP. Fermilab is Operated by Fermi Research Alliance, LLC under Contract
 352 No. De-AC02- 07CH11359 with the United States Department of Energy.

353 References

- 354 [1] B. Baller et al. Liquid argon time projection chamber research and development in the united
 355 states. *Journal of Instrumentation*, 9(05):T05005–T05005, may 2014.
- 356 [2] DUNE Collaboration, B. Abi, R. Acciarri, M. A. Acero, M. Adamowski, C. Adams, D. Adams,
 357 P. Adamson, M. Adinolfi, Z. Ahmad, and et al. The DUNE Far Detector Interim Design Report
 358 Volume 1: Physics, Technology and Strategies. *arXiv e-prints*, July 2018.
- 359 [3] A. A. Machado and E. Segreto. ARAPUCA a new device for liquid argon scintillation light
 360 detection. *JINST*, 11(02):C02004, 2016.
- 361 [4] B. Howard, S. Mufson, D. Whittington, B. Adams, B. Baugh, J.R. Jordan, J. Karty, C.T.
 362 Macias, and Pla-Dalmau. A novel use of light guides and wavelength shifting plates for the
 363 detection of scintillation photons in large liquid liquid argon detectors. *Nuclear Instruments and*
 364 *Methods in Physics Research*, 907:9–21, 2018.
- 365 [5] G. Cancelo, F. Cavanna, C. O. Escobar, E. Kemp, A. A. Machado, A. Para, E. Segreto,
 366 D. Totani, and D. Warner. Increasing the efficiency of photon collection in LArTPCs: the
 367 ARAPUCA light trap. *JINST*, 13(03):C03040, 2018.
- 368 [6] S. Coutu et al. Searching for TeV cosmic electrons with the CREST experiment. *Nucl. Phys.*
 369 *Proc. Suppl.*, 215:250–254, 2011.

- 370 [7] D. Whittington, S. Mufson, and B. Howard. Scintillation Light from Cosmic-Ray Muons in
371 Liquid Argon. *JINST*, 11(05):P05016, 2016.
- 372 [8] G. Drake P. DeLurgio, Z. Djurcic and M. Oberling. SSP User Manual. Technical report,
373 Argonne National Laboratory, 9700 S. Cass Avenue, Lemont, IL 60439 USA, 2016.
- 374 [9] L. Condat. A direct algorithm for 1-D total variation denoising. *IEEE Signal Proc. Letters*,
375 20(11):1054–1057, 2013.
- 376 [10] Prashant Shukla). Energy and angular distributions of atmospheric muons at the earth. *Nu-*
377 *clear Physics Division, Bhabha Atomic Research Centre, Mumbai 400085, India. Homi Bhabha*
378 *National Institute, Anushakti Nagar, Mumbai 400094, India*, 2018.
- 379 [11] T. Doke, H. J. Crawford, A. Hitachi, J. Kikuchi, P. J. Lindstrom, K. Masuda, E. Shibamura,
380 and T. Takahashi. Let Dependence of Scintillation Yields in Liquid Argon. *Nucl. Instrum.*
381 *Meth.*, A269:291–296, 1988.
- 382 [12] T. Doke, A. Hitachi, J. Kikuchi, K. Masuda, H. Okada, and E. Shibamura. Absolute Scintil-
383 lation Yields in Liquid Argon and Xenon for Various Particles. *Japanese Journal of Applied*
384 *Physics*, 41:1538, March 2002.
- 385 [13] R. J. Mathar. Solid angle of a rectangular plate. Technical report, Max-Planck Institute of
386 Astronomy, Königstuhl, 17, 69117 Heidelberg, Germany, 2015.
- 387 [14] M. Tanabashi et al. (Particle Data Group). The review of particle physics. *Phys. Rev. D*, 98,
388 2018.
- 389 [15] ProtoDUNE-SP Photon Detector group. Preliminary analysis.